Nature Communications

https://doi.org/10.1038/s41467-026-70106-x

Article in Press

Topology-controlled dynamic conjugated oligomers from tetra-arylsubstituted alkene building blocks

Received: 9 October 2025

Accepted: 18 February 2026

Cite this article as: Bian, Q., Zhao, Y., Zhang, C. *et al.* Topology-controlled dynamic conjugated oligomers from tetra-arylsubstituted alkene building blocks. *Nat Commun* (2026). https://doi.org/10.1038/s41467-026-70106-x

Qilong Bian, Ying Zhao, Chunhua Zhang, Yang Zhang, Yang Zhang, Zebing Zeng, Ben Zhong Tang & Sheng Xie

Topology-controlled dynamic conjugated oligomers from tetra-arylsubstituted alkene building blocks

Qilong Bian[1,2], Ying Zhao[1,2], Chunhua Zhang[3], Yang Zhang[1,2], Yang Zhang[4], Zebing Zeng[1,2*], Ben Zhong Tang[5*] and Sheng Xie[1,2*]

[1]State Key Laboratory of Chemo and Biosensing, College of Chemistry and Chemical Engineering, Hunan University, Changsha 410082, China;

[2]Shenzhen Research Institute of Hunan University, Nanshan District, Shenzhen 518000, China;

[3]School of Physics and Telecommunications Engineering, Zhoukou Normal University, Zhoukou 466001, PR China;

[4]Analytical Instrumentation Center of Hunan University, Hunan University, Changsha 410082, China;

[5]Guangdong Basic Research Center of Excellence for Aggregate Science, School of Science and Engineering, The Chinese University of Hong Kong, Shenzhen 518172, China.

Corresponding E-mails: zbzeng@hnu.edu.cn, tangbenz@cuhk.edu.cn, shengxie@hnu.edu.cn

Abstract: Topology plays an important role in polymeric materials. Herein, we present an iterative, modular approach for creating tetra-arylsubstituted alkene (TAA)-based dynamic conjugated oligomers with diverse topologies, using boronate-protected Suzuki-Miyaura coupling chemistry. The TAA building blocks involving spontaneous alkene isomerization are found to induce conformational dynamics in the conjugated backbones, exhibiting steric-controlled transitions. These transitions occur from a twisted backbone rich in cis-alkenes in the linear **PL9** oligomer, to a stretched backbone with a trans-alkene center and multiple cis-alkene end in the three-armed planar **PY12** oligomer and the four-armed 3D **PX16** oligomer. Consequently, these topological oligomers exhibit distinct photoluminescence and photochemical properties depending on their physical state. Experimental characterization and molecular dynamics simulations (MD) reveal a topology-dependent adaptive self-assembly of helices: linear **PL9** forms long flexible helical fibers with a pitch of 28 nm; planar Y-type **PY12** oligomers often occur in neural-like networks, connected by nanofibers and cell-like central aggregates; and stereo X-type **PX16** adopts short helical rod-like morphology with a mesoscopic pitch of 86 nm in crystalline phases. This work may inspire concepts and the practical construction of helical and neural-like fiber materials by altering unit topology in dynamic conjugated oligomers.

Introduction

Dynamic conjugated oligomers are mesoscale molecular materials with structural transitions that lie between small molecules and large polymers[1-4]. The precise arrangement of conjugated monomer building blocks with optoelectronic activities can give rise to secondary structures and functional properties, such as molecular recognition, organocatalysis and information encoding[5-9]. This improves the fundamental understanding of the mesoscopic assembly morphology and

macroscopic properties of oligomeric materials[10-12]. Dynamic molecular systems composed of arylsubstituted alkene building blocks exhibit the capacity to respond to external stimuli (*e.g.*, light, heat and pH), forming distinct self-assembled morphologies in the diverse material forms of frameworks, hydrogels and elastomers[13-18]. This dynamic process can also establish reversible macroscopic deformations (*e.g.*, crystal bending and stretching) that accompany switchable chemo-physical properties (*e.g.*, fluorescence)[19,20]. Such macroscopic behaviors are attributed to the *cis-trans* alkene isomerization chemistries of the tetra-arylsubstituted alkene (TAA) structures with tunable energy barriers (Figure 1A), which allow for precise manipulation of dynamic organic material systems upon stimulation[21-26]. Oligomeric materials made from flexible TAA building blocks have been shown to closely match the molecular conformation of the oligomeric backbone, forming a dynamic system[27]. Particularly, in an oligomeric system of $\geqslant$9 monomers, the TAA building blocks exhibited constant, reversible isomerization in the conjugated backbone, resulting in a spontaneous, albeit slow (taking days), constitutional dynamic process under ambient conditions. The terminal TAA groups were also found to engage in modular supramolecular TPE-TPE interactions that contribute to helical structure formation[27-29] (Figure 1B). In contrast, the corresponding di-arylsubstituted alkene units in the same polymer system only isomerized under external stimulus[27].

The backbone topology (*i.e.*, linear, star-shaped, brush-like or cyclic) is a key feature of an oligomeric system that can influence the properties of the resulting materials[30-35]. Using distinct scaffolds as the molecular core for subsequent polymerization enables the production of a subset class of oligomeric materials with both sequence accuracy and topological diversity[36-40]. These sequence- and topology-controllable oligomers are the ideal model for investigating the structure-property-function relationships, such as self-assembly dynamics. One-dimensional (1D), two-armed linear olefinic oligomers are generally flexible and facilitate the formation of helices through self-assembly. Due to the overcrowding effects, star-type oligomers (typically with three to eight arms) have been observed to exhibit high conformational rigidity in the connecting core alongside increasingly flexible surrounding arms[41,42]. This gives rise to a variety of secondary structures, including wires, rods and nets[43-45].

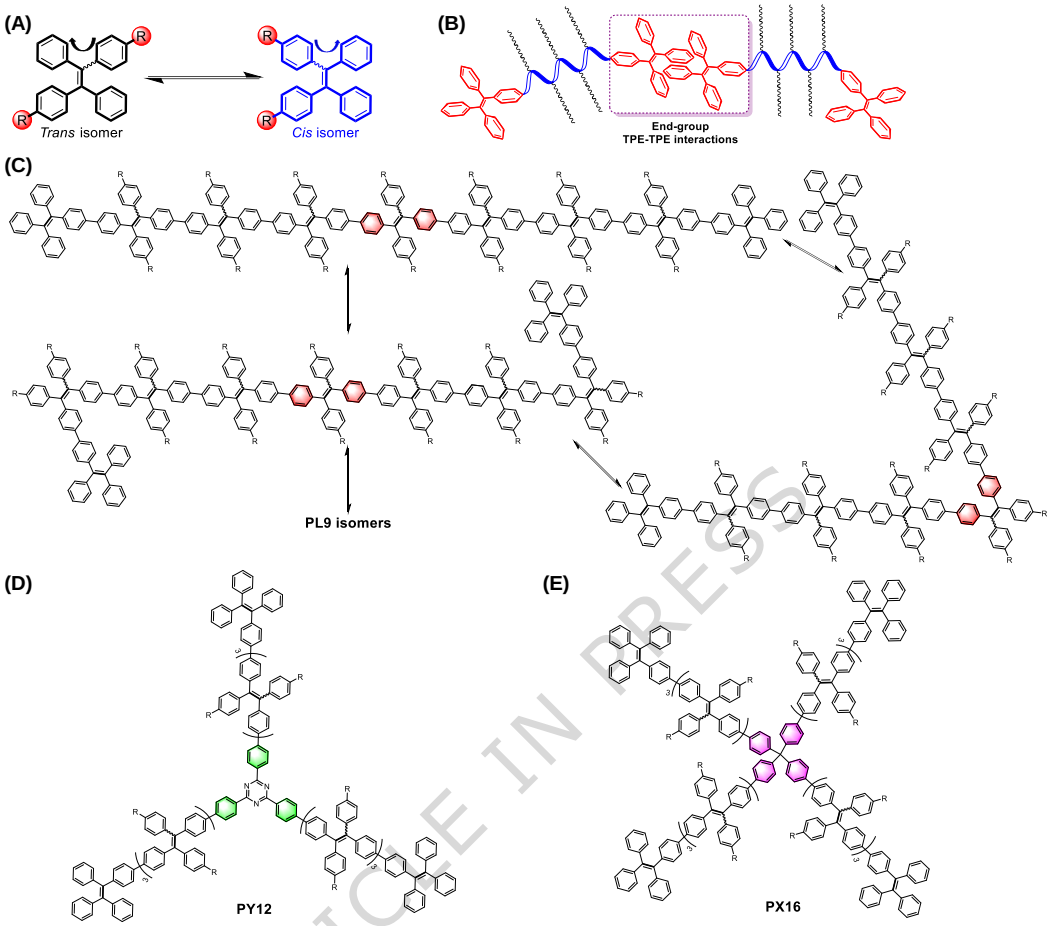

Figure 1. Schematic illustration of dynamic conjugated oligomer system with different topologies. (A) Dynamic chemistries of TAA building blocks. (B) Modular TPE-TPE interactions in supramolecular assembly. (C) 1D linear oligomer **PL9** showing dynamic conformations due to E-Z isomerization of TAA building blocks. (D) planar Y-type **PY12** and (E) stereo X-type **PX16** obtained using different core scaffold.

Drawing inspiration from the dynamic features of TAA building blocks (Figures 1A/B), herein we present a series of topology-controlled conjugated oligomers (**Pn**) via an iterative synthesis approach in the solution phase, involving MIDA-protected boronate tag-assisted Suzuki-Miyaura coupling[46-49]. The iterative synthesis process, which uses bifunctional monomer and center-linked core scaffolds, was optimized to produce 1D linear oligomer **PL9** (Figure 1C), the two-dimensional (2D) planar Y-type oligomer **PY12** (Figure 1D) and the three-dimensional (3D) X-type oligomer **PX16** (Figure 1E). Each oligomeric material constitutes a library of metastable conformers that undergo spontaneous isomerization and display dynamic interconversion, as evidenced by chiral high-performance liquid chromatography (HPLC) and 2D excitation-emission fluorescence analysis. We studied the photophysical and photochemical properties of these dynamic, topologically diverse conjugated oligomers and discussed the underlying principles. Finally, we examined the assembly process of these dynamic oligomers through solvent evaporation and re-precipitation. This reveals the relationships between molecular conformation, state-dependent properties, and supramolecular secondary structures, which are influenced by different oligomer topologies.

Results and Discussion

Preparation of Pn via iterative synthesis. These oligomers were constructed using an iterative synthesis strategy involving the cap **1** (Figure S1) and the heterobifunctional MIDA-protected building block **2** (Figure S2), which were coupled via the Suzuki-Miyaura reaction in the solution phase (Figure 2). The iterative cycle comprises three main steps in the following order: deprotection of the boronate (D), cross-coupling (C), and purification (P). The **TAA** cap **1** units are unsubstituted, which enables supramolecular TPE-TPE interactions between oligomers. To ensure the oligomers are sufficient soluble, flexible *n*-butoxy chains are introduced into the *para*-positions of **2**. The iterative synthesis of **Pn** oligomers began with a liquid-phase reaction involving cap **1** and heterobifunctional **2**. The product was then rapidly purified using flash silica gel chromatography to obtain MIDA-protected arylboronate **3** with an isolation yield of 73%. Subsequently, a library of MIDA-protected arylboronate oligomers can be obtained by repeatedly following the same D-C-P reaction cycle (**4**, 70% yield; **5**, 62% yield, Figure 2A).

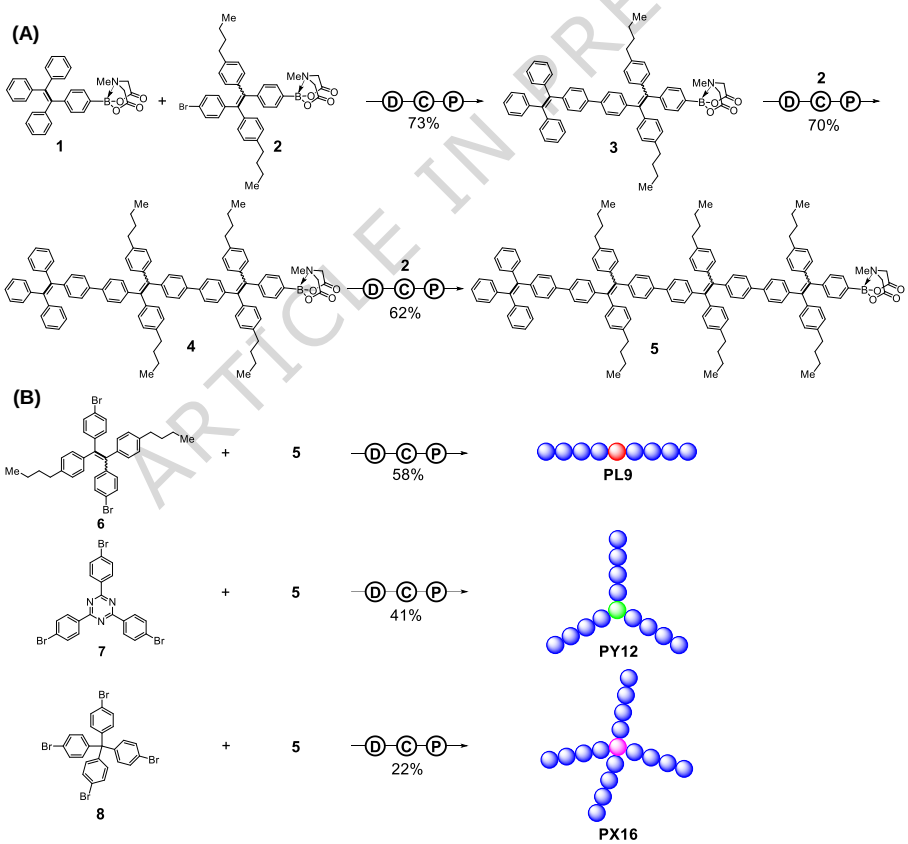

Figure 2. Iterative synthesis of precision conjugated Pn oligomers. Reaction condition for deprotection (D): [boronate] = 0.03~0.08 mM, NaOH (aq.) in THF/H_2O, 30°C, 30 min. (A) Coupling (C) reaction condition for **3**, **4** and **5**: [boronate]:[**2**] = 3:1, $Pd(OAc)_2$, Sphos, K_3PO_4 in THF, 55°C, 12 h. (B) Coupling (C) reaction condition for **PL9**: i) [**5**]:[**6**] = 2.2:1, $Pd(OAc)_2$, Sphos, NaOH in THF, 30°C for 10 min; ii) H_2O (dropwise addition), 55°C for 12 h. Coupling (C) reaction condition for **PY12**: [**5**]:[**7**] = 3.3:1, $Pd(OAc)_2$, Sphos, K_3PO_4 in 1.4-Dioxane, H_2O (dropwise addition), 90°C for 12 h. Coupling (C) reaction condition for **PX16**: [**5**]:[**8**] = 4.4:1, $Pd(OAc)_2$, Sphos, K_3PO_4 in 1.4-Dioxane, H_2O (dropwise addition), 90°C for 12 h. Purification (P) condition: flash silica gel chromatography with petroleum ether and dichloromethane as eluents.

We obtained the 1D linear oligomer **PL9** with an isolation yield of 58% by coupling the MIDA-protected arylboronate **5** and the bifunctional scaffold **6** according to the Suzuki-Miyaura protocol (Figure 2B). After optimizing the process (Table S1), we obtained the 2D planar oligomer **PY12** with an isolation yield of 41% using **5** and the planar scaffold **7**. The 3D oligomer **PX16** was formed between arylboronate **5** and the X-shaped scaffold **8**, yielding 22%. Notably, the arylboronates could be activated in situ after preparation, enabling direct coupling to the core scaffold and avoiding the need to isolate unstable boronic intermediates.

Characterization of Pn oligomers. These **Pn** oligomers were thoroughly characterized using nuclear magnetic resonance (NMR) spectroscopy (*c.f.* supplementary information), high-resolution mass spectrometry (HRMS), and elemental analysis (*c.f.* supplementary information), which demonstrated their chemical stability under ambient conditions. The purification of the oligomers was achieved through the use of flash chromatography, and their characterization as monodispersed peaks in gel permeation chromatography (GPC, Figure S3). However, the application of high-pressure liquid chromatography (HPLC) with chiral columns revealed the presence of multiple broad peaks for each **Pn**, thereby suggesting the existence of a library of metastable stereoisomers (Figure 3A/D/G). The different HPLC fractions of **Pn** oligomers were further confirmed independently as stereoisomers using matrix-assisted laser desorption ionization time-of-flight high-resolution mass spectrometry (MALDI-TOF HRMS, Figure 3A/D/G, inset). For the distinct, isolated bands of the same oligomer sample, the corresponding isotopic patterns and m/z values were found to be identical and consistent with the simulated results. **PL9** was calculated for $C_{290}H_{276}$ $[M]^+$, 3760.1665, and was found to be 3760.1542 (Figures 3A, inset). **PY12** value was calculated for $C_{405}H_{375}N_3$ $[M]^+$, 5283.9570, and was found to be 5283.9750 (Figures 3D, inset). **PX16** was calculated for $C_{537}H_{500}$ $[M]^+$, 6952.9293, and was found to be 6952.9238 (Figure 3G, inset).

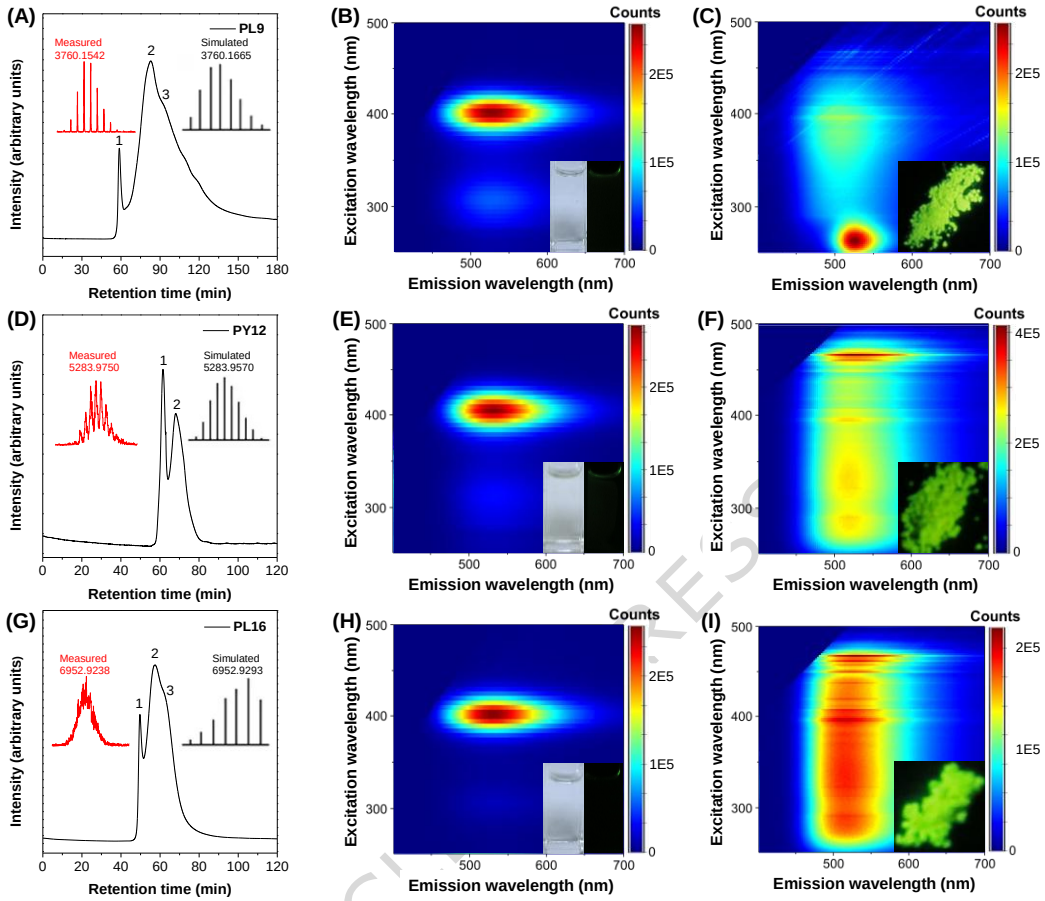

Figure 3. Molecular characterization of Pn oligomers. (A/D/G) Chiral HPLC characterization of the constitutional isomer distribution for the pristine **PL9**(A), **PY12**(D), and **PX16**(G) solution. Inset: experimentally measured (left) and computationally simulated (right) MALDI-TOF HRMS characterization for **Pn**. (Column: CHIRALPAK IF Particle size 5 μm, Dimensions 4.6 mm × 250 mm, T = 30ºC, UV = 360 nm, concentration: 1 × 10^{-6} M, V = 20 μL, 50% isopropyl alcohol/*n*-hexane, flow rate: 0.1 mL/min). (B/E/H) 2D excitation-emission fluorescence spectroscopy of the pristine **PL9**(B), **PY12**(E), and **PX16**(H) in solution state (1 × 10^{-5} M). Inset: images under natural light (right) and 365 nm irradiation (left) in THF. (C/F/I) 2D excitation-emission fluorescence spectroscopy of the pristine **PL9**(C), **PY12**(F), and **PX16**(I) in powder state. Inset: fluorescence images of the powder under 365nm irradiation.

Spontaneous isomerization of TAA monomer. The bifunctional monomer TAA **2** can exist in two interconvertible *cis*- and *trans*-alkene conformations (Figure 4A). The TAA **2** samples obtained constitute two dynamic components at thermodynamic equilibrium in solution, characterized by a chiral high-performance liquid chromatography column (HPLC, CHIRALPAK IF): **2**-1 (retention time: 118 min, 16.3%) and **2**-2 (retention time: 134 min, 83.7%) (Figure 4B). Fortunately, the HPLC system was also able to separate and purify the predominant conformer **2**-2. 2D COSY and NOESY NMR analysis revealed the predominant conformation to be the *trans*-alkene configuration (**2**-*trans*, Figure S4). However, the **2**-*trans* stereoisomer is unstable and undergoes constant interconversion via spontaneous alkene isomerization. Chiral HPLC characterization showed no substantial interconversion following isolation. However, after about 6 h, a mixture of **2**-1 and **2**-2 was observed, with a ratio of 1:5 through E-Z isomerization, essentially reaching thermodynamic equilibrium

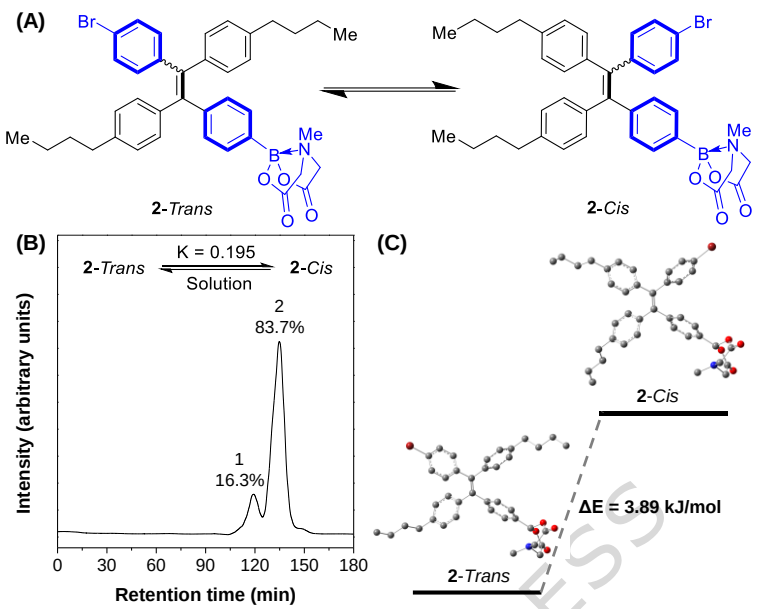

Figure 4. Dynamic interconversion of bifunctional TAA 2. (A) Reversible alkene isomerization of **2**-*Cis* ⇌ **2**-*Trans*. (B) Chiral HPLC characterization of TAA **2**, Column: CHIRALPAK IF particle size 5 μm, dimensions 4.6 mm × 250 mm, T = 30°C, UV = 360 nm, concentration: 1×10^{-6} M, V = 20 μL, 20% *n*-hexane/isopropyl alcohol, flow rate: 0.1 mL/min. (C) Computational analysis of the **2**-*Cis* ⇌ **2**-*Trans* reaction.

(Figure S5A-D). Furthermore, irradiation with 405 nm light (Figure S5E) or heating to 100°C (Figure S5F) accelerates the E-Z isomerization reaction between **2**-1 and **2**-2, achieving thermodynamic equilibrium within a mere 30 min. Subsequent computational analysis disclosed an energy difference of 3.89 kJ/mol between the two isomers at the standard state (**2**-*cis*/**2**-*trans* = 0.208, Figure 4C), which exhibited a strong correlation with the experimental equilibrium constant (K = **2**-1: **2**-2 = 16.3%: 83.7% = 0.195, Figure 4B) within the dynamically reversible **2**-2 ⇌ **2**-1 reaction model. These results suggest that the stereoisomers undergo spontaneous isomerization in solutions at ambient conditions, and can reach thermodynamic equilibrium within hours.

Stereoisomeric diversity of oligomers. The situation is complex for the topological oligomer systems formed by the iterative coupling of TAA monomers. This stereoisomeric diversity can be attributed to the inherent asymmetry of the multiple TAA units and the multiple arms present in the conjugated backbone. The same chiral HPLC characterization showed three major stereoisomeric peaks for the 1D linear oligomer **PL9** (Figure 3A), two stereoisomeric peaks for the 2D planar oligomer **PY12** (Figure 3D), and three stereoisomers for the 3D oligomer **PX16** (Figure 3G). However, due to the spontaneous *cis*-*trans* isomerization of TAA units in the topological backbone, the single peak isolated from each topological oligomer may in fact contain multiple stereoisomers. Furthermore, the presence of variations in the degree of curvature and the orientation of each arm contributes to an increase in the complexity of the oligomeric library, with minimal variation in polarity between these isomers.

It is important to note that while chromatography analysis can provide approximate distribution data for the oligomer library, it is frequently incapable of isolating the individual oligomeric isomers[6]. The 2D excitation-emission fluorescence

mapping analysis was utilized to detect different isomers in situ in real time, based on their characteristic fluorescence peak positions and intensities (Figure 3). In solution, all three oligomer libraries fluoresced weakly (see inset images), typically displaying a single excitation/emission center: 404/532 nm for **PL9** (Figure 3B), 402/536 nm for **PY12** (Figure 3E) and 402/538 nm for **PX16** (Figure 3H). The presence of a single excitation/emission center in solution can be attributed to the dynamic interconversion and isomerization of oligomers containing different *cis*-*trans* TAA building blocks. This process occurs at a rate lower than the temporal resolution of the fluorescence detection, meaning the spectra respond only to the averaged signals of all conformations over time. It is noteworthy that, in the powder state, each topological oligomer library became highly emissive and demonstrated a multitude of excitation/emission patterns. In addition to a weak one at 396/504 nm, which is similar to the solution state, the solid-state **PL9** oligomer possesses one strong excitation/emission center at 266/526 nm (Figure 3C). The planar **PY12** oligomer displays two distinct strong thin-layered excitation/emission centers (462/530 nm and 468/530 nm) and multiple weak excitation/emission centers with excitation wavelengths distributed between 260-460 nm and emission peaks at ~514 nm (Figure 3F). The **PX16** oligomer displays a greater number of excitation/emission centers, each of which subsequently intersects with adjacent centers to form a rectangular pattern region (266-470/480-580 nm) (Figure 3I). The occurrence of excitation/emission patterns with multiple centers in the powder form may be due to constrained molecular motions, which impedes intercalation isomerization between the *cis* and *trans* configurations. This results in discrete excited state energy levels forming for each oligomer with a distinct configuration. These levels manifest as multiple, distinct excitation-emission centers, the number of which increases with the number of oligomer arms.

These dynamic oligomers undergo constant isomerization. Therefore, it is not feasible to empirically validate their precise configurations. In this regard, we employed theoretical density functional theory (DFT) calculations of geometry optimization at the CAM-B3LYP-D3/6-31G(d,p) level to investigate energetically favorable molecular configurations (Figure 5). In the context of thermodynamic equilibrium, the stereoisomeric configurations that exhibit the lowest energies can be identified as the predominant components of this dynamic library. The energetically favorable **PL9** oligomer features twisted conformations on either side of a conjugated backbone consisting of consecutive *cis*-alkene TAAs, and a linear backbone structure containing a *trans*-alkene TAA in the middle (Figure 5A, left). The optimal conformation was selected out from a comprehensive library of possible configurations (Tables S2-6, Supplementary Data 1). This finding is consistent with experimental observations in analogous oligomer systems[27], indicating that the four consecutive *cis*-TAA units form a stereoregular triangular chain segment, as evidenced by in the electrostatic surface potential (ESP) image (Figure 5A, right). This structural feature is also evident in **PY12** and **PX16**. In the stable **PY12** configuration (Tables S7, Supplementary Data 2), the TAA building blocks near the flexible end groups primarily adopt an all-*cis* conformation, creating a stereoregular triangular chain segment at the periphery of each arm (Figure 5B). The three TAAs linked to the central planar scaffold adopt an all-*trans* conformation, which is likely to avoid overcrowding. Three triangular arm skeletons were formed: two faced towards one side; and one faced away from it. In the most stable **PX16** configuration (Tables S8, Supplementary Data 3), the two consecutive TAA monomers of each arm linked to the central scaffold predominantly adopt an all-*trans* conformation. This results in a near-planar, linearly extended conformation in each of the four arms (Figure 5C). The terminal TAA groups in the peripheral regions primarily adopt a *cis*-configuration, forming triangular segments, as in **PY12** and **PL9** (Figure 5C, right). Clearly, the number of oligomer

arms modulates the flexible conformational dynamics of conjugated backbones and thus alleviates spatial site resistance efficiently. Apparently, HOMO-LUMO analysis moreover revealed that the conjugated extension of **PL9**, **PY12**, and **PX16** predominantly occupies four consecutive TAA monomers in a similar manner, producing a similar discrete, stereoregular triangular segment (Figure S6).

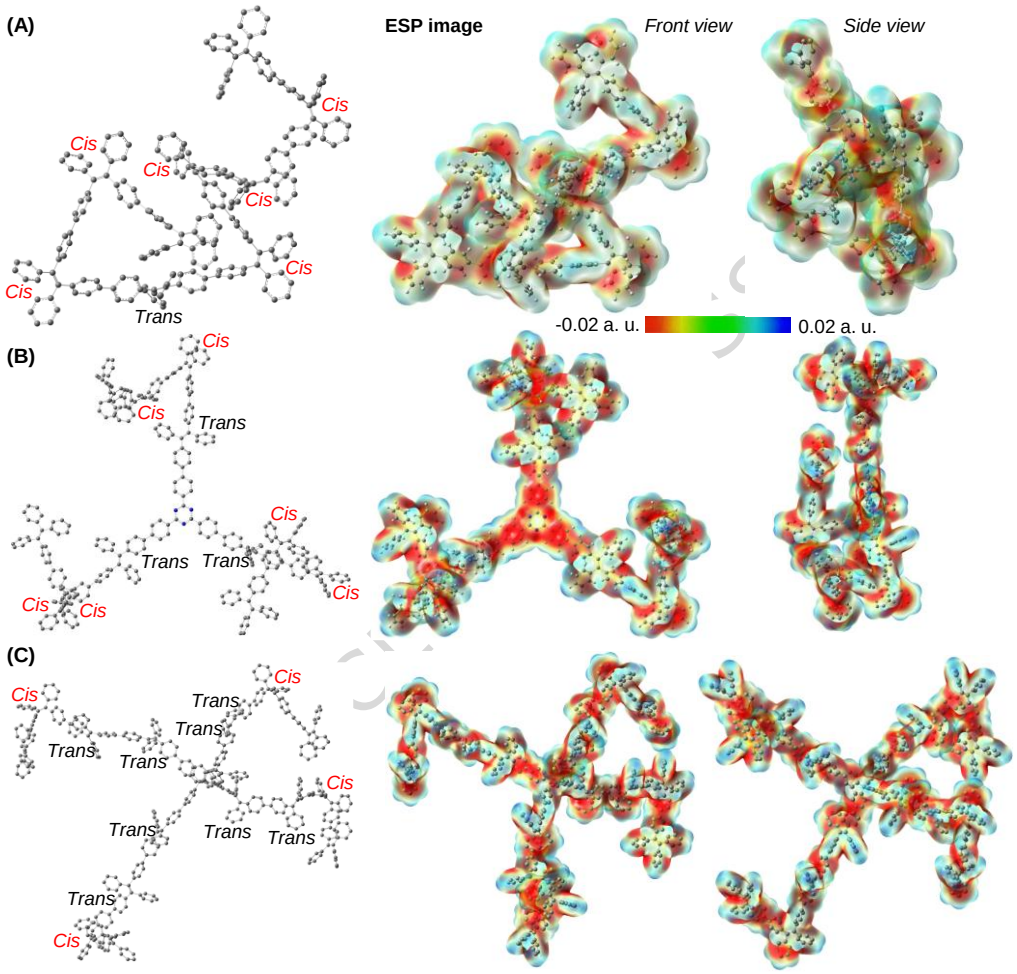

Figure 5. Dominant molecular conformations and electrostatic surface potential (ESP) images of Pn oligomers by theoretical calculations. a) Conformation (left), front view (middle), and back view (left) of corresponding ESP images of the dominant **PL9** oligomer. b) Conformation (left), front view (middle), and side view (left) of corresponding ESP images of the dominant **PY12** oligomer. c) Conformation (left), front view (middle), and side view (left) of corresponding ESP images of the dominant **PX16** oligomer. Calculations were carried out at the CAM-B3LYP-D3/6-31G(d,p) level. Aliphatic chains and hydrogen atoms are omitted for clarity.

State-dependent optical properties indicating constitutional dynamics. We characterized the optical properties of the **Pn** oligomers as molecularly dissolved in dilute THF solution (Figures 6A/B), as micro/nano aggregates in solution (Figures 6C/D), and as solid powder (Figures 6E/F). The maximum light absorption of **Pn** oligomers with different topologies changes only slightly. This is primarily because the conjugate extensions of linear **PL9** predominantly occupy four consecutive TAA monomers, and **PY12**/**PX16** oligomers have four TAA monomers in each arm, forming a comparable conjugation system (Figure S6). **PY12**'s electronic ground state transitions are primarily derived from HOMO-LUMO, accounting for over 85% (Figure S7, Table S10). In contrast, the contributions from higher energy

orbitals, as determined by TD-DFT methods (Figure S7, Tables S9/S11), are significant for **PL9** and **PX16**. Furthermore, natural transition orbitals (NTO) analysis (Figure S8) indicates that the S_1 state of **PL9** and **PX16** exhibits an alternating distribution of holes and electrons throughout the conjugated backbone of the entire molecule. In contrast, the hole-electron distribution in **PY12** exhibits localized spatial separation, with holes predominantly concentrated on the tris(phenyl)triazine moiety, while electrons are primarily localized on the three arms. It is noteworthy that the maximum absorption of the **Pn** oligomers exhibited a direct correlation with the degree of aggregation. For the single molecular species, aggregates, and powders, the maximum absorption was found at 358, 393 and 370 nm for **PL9**, 363, 393 and 370 nm for **PY12**, and 354, 387 and 370 nm for **PX16**, respectively (Table 1). These aggregation-induced effects are reversible upon re-solubilization. These topological oligomers possess multiple long aliphatic chains on each arm and do not demonstrate significant donor-acceptor interactions. This phenomenon is likely attributable to a shift in the conformational distribution of the stereoisomers across varying physical states. This hypothesis is further substantiated by the absence of an aggregation-induced red shifts in the absorption spectra of control experiments involving symmetrical tetraphenylethylene (TPE) (Figures 6A/C/E, black). Subsequent DFT calculations and MD simulations suggest that the self-assembled topological oligomer is prone to adopting a planar conformation with multiple arms that bend to accommodate close packing (Figure S9).

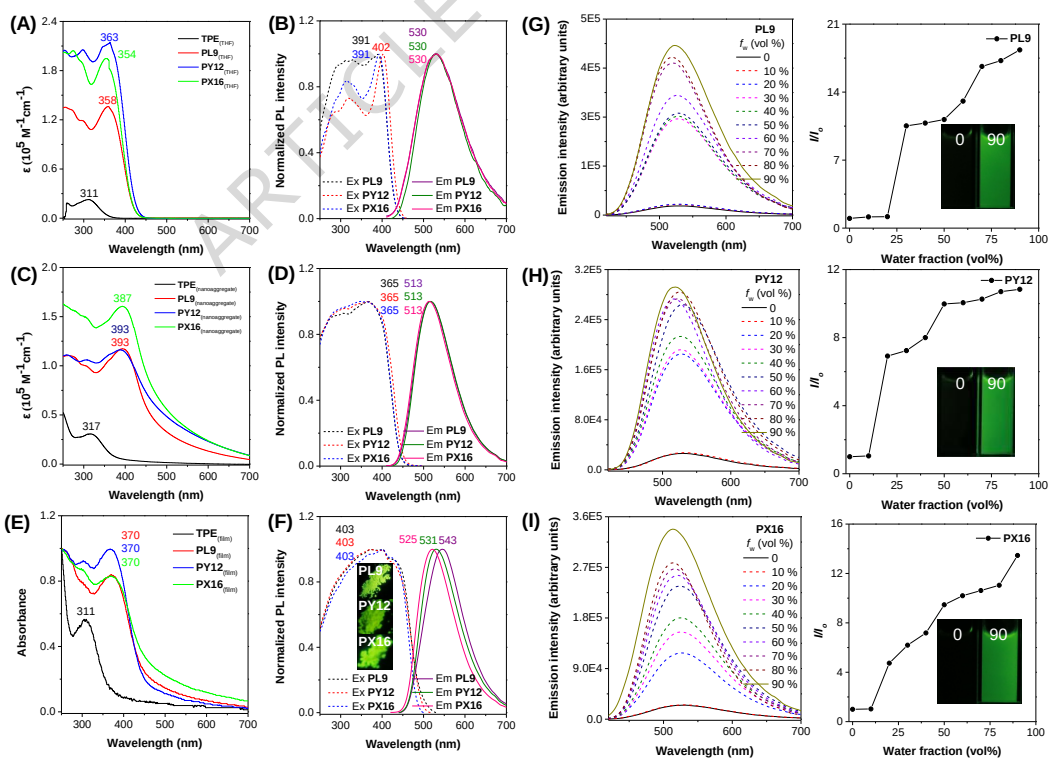

Figure 6. **Photophysical properties of Pn oligomers at different materials states.** (A/C/E) UV-vis absorption of **Pn** as (A) molecularly dissolved in THF solutions (1×10^{-5} M), as (C) disperse nanoaggregates in mixed 90 vol% water/THF solutions, and as (E) solid powder/films. (B/D/F) Corresponding steady fluorescence excitation (dot dash) and (solid line) emission spectra of **Pn** as (B) molecularly dissolved in THF solutions (1×10^{-5} M), as (D) disperse nanoaggregates in mixed solutions, and as (F) solid powder. Inset: fluorescence image in powder under 365 nm light irradiation. (G/H/I) Fluorescence spectra of (G) **PL9**, (H) **PY12**, and (I) **PX16** in series THF/water mixtures with different

water fractions (f_w) and corresponding plots of relative emission peak intensity (I/I_0) versus f_w. I_0 was the peak intensity when f_w = 0. Inset: fluorescence image in solvents of f_w = 0 and 90 under 365 nm irradiation. Concentration: 1×10^{-5} M. Excitation wavelength: 370 nm.

The state-dependent optical properties of oligomers were also observed in the fluorescence characterization (Figure 6, Table 1). The excitation maxima were significantly different from the adsorption maxima in the molecularly dissolved state (Figure 6B), as dispersed aggregates in mixture solutions (Figure 6D) and the powder state (Figure 6F). This finding suggests that the oligomers underwent substantial conformational changes upon excitation at different states, which is likely attributable to dynamical E-Z isomerization of the conjugated backbone. Despite their different topologies, the fluorescence peaks of **Pn** remain constant at 530 nm in solution (Figure 6B) and 513 nm in dispersed aggregates (Figure 6D). The corresponding powders exhibited a slight blue shift as the number of molecular arms increased (**PL9**, 543 nm; **PY12**, 531 nm; **PX16**, 525 nm) (Figure 6F). These oligomers exhibit analogous electronic systems in their photoexcited state, which corresponds with the fundamental chain segment, as determined by DFT calculations (Figure S6).

Table 1. Photophysical properties of **Pn** oligomers at different states.

	λ_{abs}, λ_{ex} /λ_{em} [nm] (Φ_F %)[a]			τ [ns] (k_r [10^8 s^{-1}], k_{nr} [10^8 s^{-1}]) [b]		α(AIE)[c]
	THF solution	Aggregate[d]	Powder	Aggregate[d]	Powder	
PL9	358, 391/530 (3)	393, 365/513 (66)	370, 403/543 (63)	3.1 (2.1, 1.1)	3.3 (1.9, 1.1)	18
PY12	363, 402/530 (2)	393, 365/513 (93)	370, 403/531 (96)	2.9 (3.2, 0.2)	3.4 (2.8, 0.1)	11
PX16	354, 391/530 (2)	387, 365/513 (83)	370, 403/525 (80)	3.3 (2.5, 0.5)	3.3 (2.4, 0.6)	13

[a]Absolute quantum yields measured by an integrating sphere. [b]k_r: radiative decay rate, k_{nr}: nonradiative decay rate. [c]Estimated by I/I_0, corresponding to Figure 6G/H/I. [d]Reprecipitation in 10 vol% THF/H_2O, corresponding to Figure 6C/D.

The energy band gaps of oligomers gradually increase for the dominant configurations of these dynamic oligomers as the number of oligomeric arms increases (**PL9**-1: 3.38 eV, **PY12**-1: 3.39 eV, and **PX16**-1: 3.59 eV). The HOMO/LUMO of **PL9**-1 encompasses the central five monomeric units of the linear conjugation. This distribution is predominantly constrained to the localized system within the central region of the twisted skeleton and does not expand with an increase in monomer units. In the three-armed planar oligomer **PY12**-1, the HOMO of is primarily distributed across the four monomeric units on one of the arms, while the LUMO is predominantly located on the central 2,4,6-triphenyl-1,3,5-triazine scaffold and one monomeric unit that overlaps with the LUMO. This phenomenon is primarily caused by the spatial site resistance exhibited by the three-arm oligomers, which results in the central connecting unit being unequally conjugated to each arm. In contrast, the HOMO/LUMO of the four-armed oligomer **PX16**-1 undergoes significant spatial separation, primarily between two arms in different positions, due to the non-conjugated center scaffold obstructing the off-domain orbitals of the entire system.

These topological oligomers exhibit distinct aggregation-induced emission (AIE) properties, despite of similar electronic systems. Their dilute solutions showed weak fluorescence, with quantum yields (Φ_F) of 2~3% and a fluorescence lifetime of less than 1 ns (Figure S10). This phenomenon is primarily due to the active molecular motions and dynamic, reversible photochemical transformations of the TAA building blocks, which dissipate the photoexcited

state energy effectively. Their fluorescence increased significantly upon aggregation, reaching Φ_F = 66%, 93% and 83% for **PL9**, **PY12**, and **PX16** in the aggregated state, and 63%, 96% and 80% for **PL9**, **PY12**, and **PX16** in the powder state, respectively (Table 1). Time-resolved fluorescence analysis revealed that the increase in fluorescence was primarily caused by a significant increase in the radiative rate and a reduction in the nonradiative decay rate. Interestingly, the three- and four-armed oligomers **PY12** and **PX16** exhibited significantly higher fluorescence efficiency in aggregated states than the two-armed oligomer **PL9**. Particularly, **PY12** has a fluorescence efficiency of 96% in the solid state, which is almost the highest for TAA-based polymeric materials. This is mainly due to the suppression of the spatial non-radiative transition channel (k_{nr}), caused by the site barrier effects of multiarmed oligomers. These effects enhance the rigidity of the oligomers, rendering them less susceptible to distortion and conformational changes.

The self-assembly of these dynamic oligomers to form supramolecular structures was next investigated in a precipitation process in mixed solutions (Figure 6G/H/I). These oligomers were first dissolved in a highly soluble THF solution (10 μM). Then, a poorly soluble in water was added to induce molecular aggregation. As shown (Figure S11), UV-vis absorption tails off, suggesting the formation of oligomeric aggregates due to Mie diffraction, when the solvent content exceeds a certain level (30 vol% for **PL9**, 20 vol% for **PY12** and **PX16**). This is accompanied by the emergence of fluorescence emission, which intensifies further as the water content of the mixtures increases. Due to the complexity of the oligomer aggregation system, the luminescent molecular states of different oligomer species are recognizable in the 2D excitation-emission fluorescence mapping, which shows that the emission color and intensity change with the degree of oligomer aggregation (Figure S12). Compared with **PL9** (30 vol% water content), both the three-armed **PY12** (20 vol% water content) and the four-armed **PX16** (20 vol% water content) demonstrated greater sensitivity to molecular aggregation, due to the increased interacting surfaces when a poor solvent is added. However, they exhibited lower fluorescence enhancement, with α_{AIE} (I_{max}/I_0) reaching 18-, 11- and 13-fold for **PL9**, **PY12**, and **PX16**, respectively (Table 1). This suggests that the structural topology is a fundamental factor in modulating the fluorescence dynamics of these aggregation-induced emission systems, which may be correlated with the molecular motion modes.

Topology-dependent self-assembly of helical and neural-like networks. These topological polymers with dynamic polyolefin backbones can self-assemble into secondary structures with diverse morphologies[36-40] (Figure 7). Note, the evaporation of **Pn** solutions at high concentrations (>100 μM) typically resulted in the formation of bulky amorphous aggregates (Figure S13). At low concentrations, the formation of regular supramolecular structures could be achieved, for instance, by gradually evaporating a toluene solution of **Pn** (1 μM) onto silicon wafer substrates. Atomic force microscopy (AFM) revealed that the linear **PL9** self-assembled into helical nanofibers with a uniform thread pitch (Tp) of approximately 28 nm, typically measuring 118-121 nm in width (W), 3 nm in height (H) (Figure 7A). These homogeneous oligomeric fibers were also observed by scanning electron microscopy (SEM) at a viewing angle of 10 μm (Figure 7D, Figure S14A/D). The 2D planar **PY12** oligomers were observed to self-assemble into nanowires using AFM, but did not exhibit a pronounced helical structure, with a width of 186-192 nm and a height of 3 nm (Figure 7B). As indicated by SEM, the **PY12** oligomers displayed a neural-like, multilevel network structure, which is of particular significance (Figure 7E, Figure S14B/E). The formation of this network structure may be attributed to the misaligned stacking of nanowires during the growth process, resulting in the emergence of bifurcation points within the nanowire

assembly. Concurrently, directionality is exhibited in the assembly of triangular planar **PY12** oligomers, resulting in the sustained extension of nanowires in multiple directions along misaligned stacking. Subsequent to this, the formation of nodes is initiated by the alignment and stacking of additional nanofibers, resulting in the establishment of a nanonetwork structure that bears a resemblance to that of a neural network.

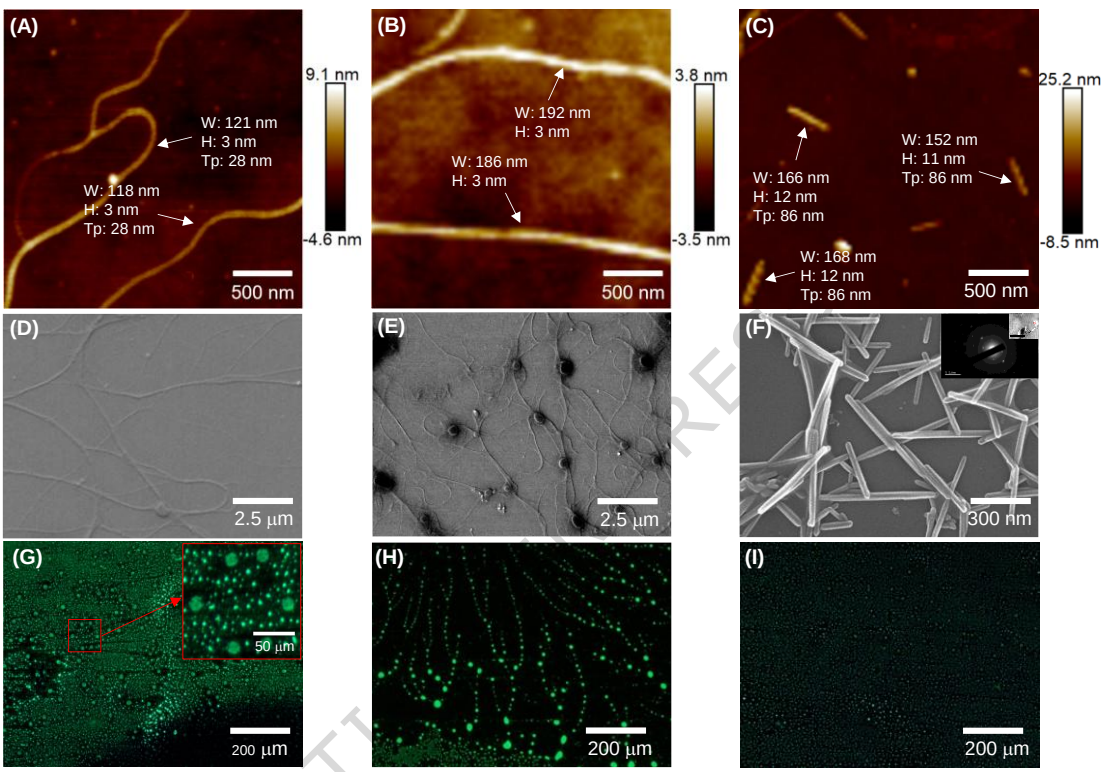

Figure 7. Self-assembly of Pn oligomers. (A-C) AFM Characterization of assembled structures by evaporation of 1 μM toluene solution on silicon wafer for **PL9** (A), **PY12** (B), and **PX16** (C). (D-F) Corresponding SEM characterization of assembled structures by evaporation 1 μM toluene solution on silicon wafer for **PL9** (D), **PY12** (E), and **PX16** (F). Inset: TEM characterization of nanorods. (G-I) Positive fluorescence microscope characterization of assembled structures by evaporation of 10 μM toluene solution on clean quarz glass substrates for **PL9** (G), **PY12** (H), and **PX16** (I). Excitation wavelength: 330-380 nm. H: height, W: width, Tp: thread pitch. SEM samples were sprayed with platinum for 15 seconds to increase their electrical conductivity.

Surprisingly, the 3D **PX16** oligomers self-assembled into straight, linear nanorods with uniform helicity. These regular rods were 152-168 nm wide, 11-12 nm high, and had an average Tp of around 86 nm (Figure 7C). Using SEM at a comparable magnification, the supramolecular helicity could also be observed in these twisted nanorods (Figure 7F, Figure S14C/F). Further transmission electron microscopy (TEM) characterization revealed a regular diffraction pattern, indicating crystalline phases for these nanorods (Figure 7F, inset). However, subsequent powder X-ray diffraction (PXRD) revealed that the patterns of oligomer **Pn** all exhibited broad peak envelopes (Figure S15). This result indicates that all three lack a long-range ordered three-dimensional crystal structure in the powder state, suggesting the possible presence of short-range ordered structures.

Following the sequential evaporation of a toluene solution of **Pn** oligomer (1 μM) onto a quartz glass substrate, circular dichroism (CD) signals from self-assembled **Pn** oligomers with distinct topological structures were observed via UV

circular dichroism spectroscopy (Figure S16). Supramolecular assemblies formed by the 2D planar oligomer **PY12** exhibited no significant chiral signal, whereas assemblies formed by the 1D linear oligomer **PL9** and the 3D oligomer **PX16** displayed weak chiral signals. This phenomenon can be attributed to the differential inductive capabilities of molecular geometries in influencing the formation of supramolecular helical chirality.

Different assembly behaviors were also observed for topology-controlled oligomers under fluorescence microscopy after the slow evaporation of a toluene solution of **Pn** oligomers (10 μM) on quartz glass substrates. The slow evaporation rate of toluene and its weak Marangoni effect allowed molecules sufficient time to stack stably, thereby achieving long-range ordered arrangements through intermolecular van der Waals forces and π-π stacking interactions. The 1D linear **PL9** oligomers assembled into two different sizes of microsphere in close proximity: the small, evenly distributed particles likely represent one polymer per particle (diameter = 2 μm), while the medium-sized particles are fused with several oligomers (diameter = 13 μm) (Figure 7G). Similarly, the 3D **PX16** oligomers self-assembled into regular microspheres of a comparable size (Figure 7I). Interestingly, the 2D planar **PY12** oligomers formed homogeneous microspheres, but created dendritic, multifurcated particle patterns at interfaces (Figure 7H). The furcation node of each dendritic structure was significantly larger than that of the self-assembled microspheres. These interconnected structures showed similar furcation patterns, which correlated with the neural-like networks observed under SEM (Figure 7E). This may be attributed to the geometric constraints imposed by the rigid central scaffold, which favors extending the self-assembly to the exterior and thereby forming a multibranched network. Here, the dimensional structure of the oligomer unit determines the available 'connection points and patterns' for self-assembly. The strength of the intermolecular forces and the orientation of the molecular conjugation determine the manner in which these connections are formed.

Molecular interactions behind dynamic assembly via MD simulation. We successfully cultivated needle-like microcrystals from the **PX16** solution; however, we were unable to resolve the precise molecular conformation through single crystal X-ray diffraction, probably due to the packing disorder and ultimately weak diffraction intensity. To understand the dynamic self-assembly behaviors of **Pn** oligomers in forming modular helices and neural network-like structures, MD simulations were instead used to investigate possible oligomer stacking within the most prevalent space groups (*C2/c*, *P-1*, $P2_1$, $P2_1/c$, $P2_12_12_1$, *Pbca*, *Pbcn* and $Pna2_1$), which account for over 80.5% of organic stacking patterns (Table S12, and Figures S17-20 for **PL9**; Table S13, and Figures S21-23 for **PY12**; Table S14, and Figures S24-27 for **PX16**). The MD simulations can help to reveal how molecules in a solvent transform into optimal structures in potential crystalline states. The following discussion of the dynamic helix (**PL9**-1, *P-1* space group; **PX16**-1, $P2_1$ space group) and neural network (**PY12**-1, $P2_1$ space group) formation processes (Figure 8) mainly uses the best stacking models that take into account the total energy and matter density issues in the self-assembly process (Figure S28).

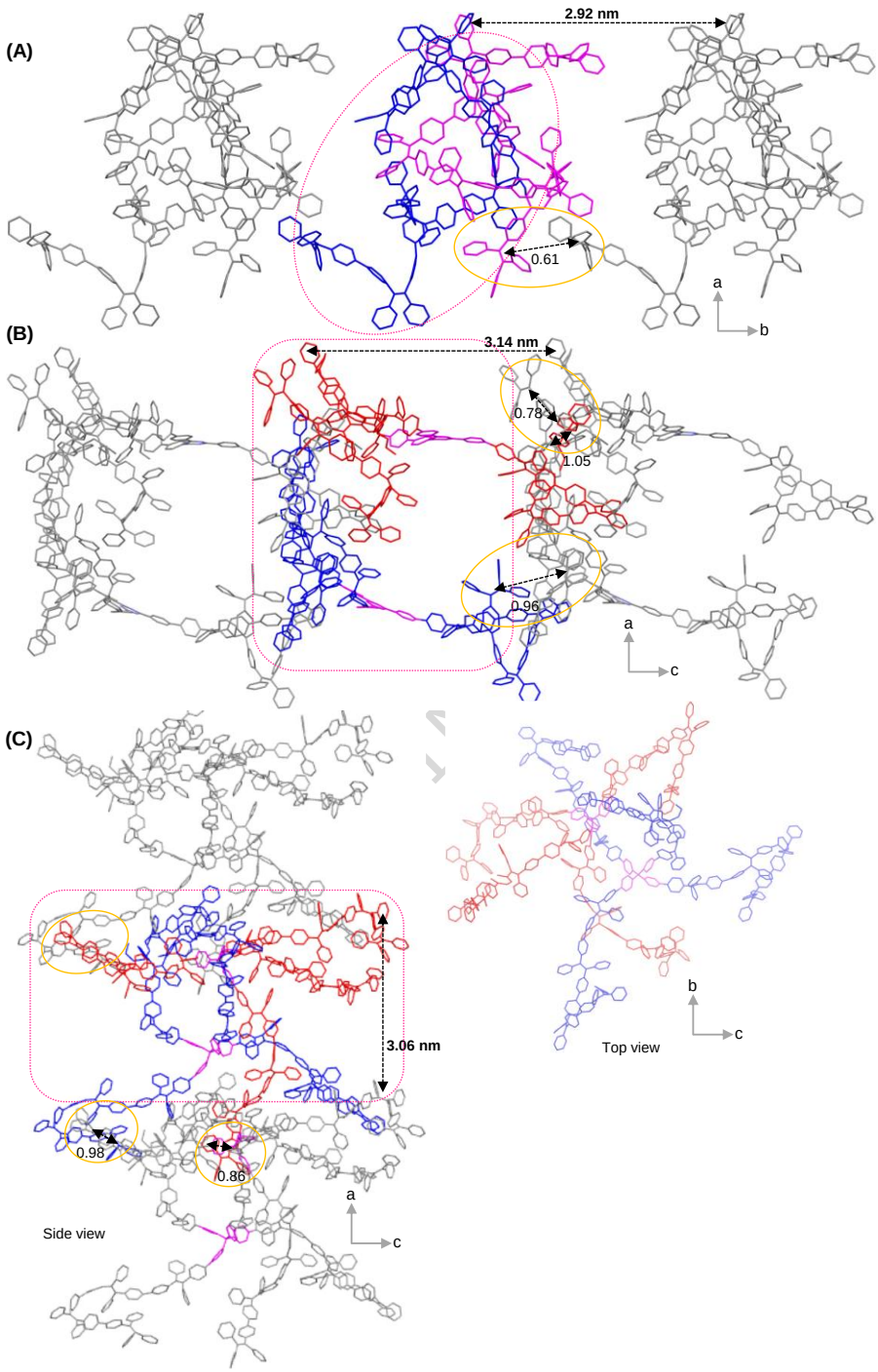

Figure 8. Molecular interactions in the supramolecular Pn assembly via MD simulation. (A) Molecular packing modelling of cell growth along the *b* axis of **PL9**-1 oligomer in the *P-1* space group, showing two molecules in a unit cell. (B) Molecular packing modelling of cell growth along the *c* axis of **PY12**-1 oligomer in the $P2_1$ space group, showing two molecules in a unit cell. (C) Molecular packing modelling of cell growth along the *a* axis of **PX16**-1 oligomer in the $P2_1$ space group, showing three molecules in a unit cell.

As can be seen (Figure 8), these flexible oligomers underwent assembly, changing from a freely-stretching state in the solvent to form a highly distorted conjugated backbone and undergoing significant changes in spatial conformation. In particular, the modular TPE-TPE interactions between the terminal groups were observed to be essential for stabilizing

the linkage between neighboring oligomers (black arrows) and unit cells (yellow circle), thereby guiding regular assembly. At the supramolecular level, two conformationally similar two-armed linear **PL9**-1 oligomers were stacked on top of each other in a cross-stacking configuration to form a single cell with a curved, linear shape, with a distance of 2.92 nm between cells (black dashed arrow, Figure 8A). The cells then continued to grow along the *b*-axis in an upper and lower staggered stacking pattern (Figure S28A). Thus, the secondary helical structure is likely to be formed through the aggregation of oligomers in the *P-1* crystalline state. Similar helical conformational features were also observed in the crystalline states of other space groups (Figures S17-20). Interestingly, the three-armed planar **PY12**-1 oligomers consist of two face-to-face slip-stacked planar molecules in a single cell. This forms a U-shaped cell with a distance of 3.14 nm between the cells (black dashed arrow, Figure 8B), which continues to grow in a dislocated stacking pattern along the *c*-axis (Figure S28B). Thus, these structural features of forming helix can be envisioned in the $P2_1$ and other space groups (Figures S21-23). A discernible pattern of supramolecular aromatic interactions was observed (yellow circle, Figure 8B): one arm of an oligomer in one unit cell forms a regular complex with two different arms of two oligomers in the next unit cell through multivalent TPE-TPE-TPE interactions. These interactions direct the infinite outward expansion of the oligomer, resulting in the formation of a porous network. Typically, these four-armed **PX16**-1 oligomers cross-stacked with each other via arm-arm entanglements, forming twisted pillars with a unit cell distance of 3.06 nm (side view, Figure 8C). From the top view, the central scaffolds of the oligomers were closely arranged and their peripheral arms stretched outwards to form an umbrella-shaped superstructure (top view, Figure 8C). Thus, a helical structure can be constructed through the regular assembly of oligomers in the crystalline state of the $P2_1$ and other space groups (Figure S28B, Figures S24-27). This suggests principles for reconstructing nanorods using MD simulation.

These dynamic oligomer models feature a central scaffold with different topologies, as well as multi-armed conjugation backbone system with reversible cis/trans isomerization chemistry. This gives the individual oligomers high flexibility, leading to the emergence of diverse, topology-dependent secondary structures. The TAA units in the long backbone ($n \geq 5$) are generally prone to adopting the *cis*-conformation, forming a specific twisted chain backbone segment consisting of four to five TAA units in the energy minimum state. However, the central scaffolds modulated the backbone system, producing *trans*-rich TAA units in close proximity to the central scaffolds due to steric effects. In the self-assembly process, the oligomers rotate and stretch as they stack to form twisted fibers with a helical structure. This process is guided by terminal TPE-TPE interactions and facilitated by multiple alkyl chains along the oligomer backbone. Importantly, this oligomeric system gave rise to unusual secondary supramolecular structures. Under controlled conditions, the **PY12** oligomers assembled to create a mesoscale fiber-cell network, mimicking a biological neural system. The **PX16** complex oligomers formed uniform helical nanorods in a crystalline state. These interesting and rare oligomer models warrant further investigation.

In this work, a class of TAA-based dynamic conjugated oligomers with different topologies was constructed via a liquid-phase iterative synthesis. This oligomeric material system with dynamic conformations exhibited state-dependent fluorescence emission and topology-dependent helix self-assembly. This system can be utilized as an oligomer model to study the effects of dimensions on the structure, properties and functions of molecular materials. These dynamic oligomer models feature a central scaffold with different topologies, as well as a multi-armed conjugation backbone system with

reversible *cis*/*trans* isomerization chemistry. This characteristic endows the individual oligomers with a high degree of flexibility, which, in turn, gives rise to the emergence of diverse, topology-dependent secondary structures. The linear **PL9** oligomers self-assemble into helical nanowires with a pitch of more than 28 nm, the planar **PY12** oligomers self-assemble into a neural network-like structure, and the steric **PX16** oligomers form helical nanorods with a pronounced crystalline phase and a pitch of 86 nm. Mechanistic investigations have revealed the critical role of a stereoregular, *cis*-rich chain segment involving four to five TAA units in the long-chain backbone of **PL9**. This process is further modulated by the central scaffold in **PY12** and **PX16**, thereby enabling the adaptive assembly of *trans*-rich secondary structures via *cis*-to-*trans* TAA isomerization. Terminal TPE-TPE interactions and the effects of multiple alky chain from the backbone are also discussed during the diverse self-assembly processes that lead to the formation of crystalline helical nanorods and neural-like fiber-cell networks. This study of dynamic conjugated oligomers explores how the topology of an oligomer influences its conformation, properties, and function. This work may inspire concepts and the practical construction of helical and neural-like fiber materials by modifying the topology of units.

Methods

The general methods used in this study, including the synthesis and characterization of oligomers, are described in the supplementary information.

Data Availability

The data supplementary the findings of this study are available in the article. All data are available from the corresponding author upon request. Source Data are provided with this manuscript. The data in this manuscript do not include clinical data or third-party data; all data originate from the authors' experimental work. The experimental characterization and computational data generated in this paper are provided in the supplementary information.

References

1. Hemminger, J. *et al.* From quanta to the continuum: oppor tunities for mesoscale science. U.S. Department of Engery, 3-11 (Argonne National Laboratory, United States, 2012).
2. Hughes, J., Tran, C. & Rappporteurs, J. A. Mesoscale chemistry: a workshop summary. National Academies Press, 2-8 (Washington, DC 2015).
3. Tu, Y., Zhao, Z., Lam, J. W. Y. & Tang, B. Z. Aggregate science: much to explore in the meso world. *Matter* **4**, 338-349 (2021).
4. Zhang, B., Watuthanthrige, N. D. A., Wanasinghe, S. V, Averick, S. & Konkolewicz, D. Complementary dynamic chemistries for multifunctional polymeric materials. *Adv. Funct. Mater*. **32**, 2108431 (2022).
5. Ni, Z. *et al.* Mesopolymer synthesis by ligand-modulated direct arylation polycondensation towards *n*-type and ambipolar conjugated systems. *Nat. Chem.* **11**, 271-277 (2019).

6. Genabeek, B. V. *et al.* Properties and applications of precision oligomer materials; where organic and polymer chemistry join forces. *J. Polym. Sci.* **59**, 373-403 (2021).
7. Shi, Q., Deng, Z., Hou, M., Hu, X. & Liu, S. Engineering precise sequence-defined polymers for advanced functions. *Prog. Polym. Sci.* **141**, 101677 (2023).
8. Murphy, E. A., Zhang, C., Bates, C. M. & Hawker, C. J. Chromatographic separation: a versatile strategy to prepare discrete and well-defined polymer libraries. *Acc. Chem. Res.* **57**, 1202-1213 (2024).
9. Pasgrimaud, C. *et al.* Synthesis of electron-deficient BisAzaCoroneneDiimide-conjugated polymers by light-locking dynamic covalent bonds. *J. Am. Chem. Soc.* **147**, 12218-12227 (2025).
10. Anderson, P. W. More is different. *Science* **177**, 393-396 (1972).
11. Barua, H., Svärd, M., Rasmuson, Å. C., Hudson, S. P. & Cookman, J. Mesoscale clusters in the crystallisation of organic molecules. *Angew. Chem. Int. Ed.* **63**, e202312100 (2024).
12. Zhang, Y., Xie, S., Zeng, Z. & Tang, B. Z. Functional scaffolds from AIE building blocks. *Matter* **3**, 1862-1892 (2020).
13. Xu, G. *et al.* α-Cyano triaryl[3]radialene: unsymmetrical stereo-configuration, clustering-enhanced excimer emission, and radical-involved multimodal information switching. *Angew. Chem. Int. Ed.* **62**, e202305011 (2023).
14. Wang, X. *et al.* Photoelectromagnetic responsive adaptive porous frameworks through dynamic covalent chemistry of tetraarylethylene-backboned aryldicyanomethyl radicals. *Angew. Chem. Int. Ed.* **62**, e202301719 (2023).
15. Liu, H. *et al.* A photoelectromagnetic 3D metal-organic framework from flexible tetraarylethylene-backboned ligand and dynamic copper-based coordination chemistry. *Small* **20**, 2306956 (2024).
16. Meng, S. *et al.* Anisotropic flexibility and rigidi fication in a TPE-based Zr-MOFs with scutopology. *Nat. Commun.* **14**, 5347 (2023).
17. Wang, S., Zhang, Q., Wang, Z., Guan, S. & Zhang, X. Tetraphenylethylene-based hydrogen-bonded organic frameworks (HOFs) with brilliant fluorescence. *Angew. Chem. Int. Ed.* **62**, e202315382 (2023).
18. Li, C., Zhao, W., He, J. & Zhang, Y. Topology controlled all- (meth) acrylic thermoplastic elastomers by multi-functional lewis pairs-mediated polymerization. *Angew. Chem. Int. Ed.* **63**, e202401265 (2024).
19. Irie, M., Fukaminato, T., Matsuda, K. & Kobatake, S. Photochromism of diarylethene molecules and crystals: memories, switches, and actuators. *Chem. Rev.* **114**, 12174-12277 (2014).
20. Zhou, Z. *et al.* Spiro-functionalized diphenylethenes: suppression of a reversible photocyclization contributes to the aggregation-induced emission effect. *J. Am. Chem. Soc.* **141**, 9803-9807 (2019).
21. Xie, Y. & Li, Z. Recent advances in the Z/E isomers of tetraphenylethene derivatives: stereoselective synthesis, AIE mechanism, photophysical properties, and application as chemical probes. *Chem. Asian J.* **14**, 2524-2541 (2019).

22. Huang, Y. *et al*. Tuning proapoptotic activity of a phosphoric-acid-tethered tetraphenylethene by visible-light-triggered isomerization and switchable protein interactions for cancer therapy. *Angew. Chem. Int. Ed.* **61**, e202208378 (2022).

23. Huang, Y., Zhang, G., Zhao, R. & Zhang, D. Tetraphenylethene-based cis/trans isomers for targeted fluorescence sensing and biomedical applications. *Chem. Eur. J.* **29**, *e202300539* (2023).

24. Liu, X., Li, Y., Li, X. & Hahn, F. E. Photoinduced E to Z isomerization of tetraphenylethylene derivatives within organometallic supramolecular assemblies. *Sci. China Chem.* **64**, 1709-1715 (2021).

25. Yu, X. Trans/cis-stereoisomers of triterpenoid-substituted tetraphenylethene: aggregation-induced emission, aggregate morphology, and mechano-chromism. *Nanoscale* **13**, 15257-15266 (2021).

26. Nie, X. *et al.* Kinetic and thermodynamic control of tetraphenylethene aggregation-induced emission behaviors. *Aggregate* **3**, e165 (2022).

27. Bian, Q. *et al.* Iterative synthesis of dynamic conjugated oligomers displaying length-dependent configuration metastability, state-dependent properties, and helix emergence. *Angew. Chem. Int. Ed.* **64**, e202505703 (2025).

28. Xia, Q. *et al.* Direct visualization of chiral ampli fication of chiral aggregation induced emission molecules in nematic liquid crystals. *ACS Nano* **15**, 4956-4966 (2021).

29. Li, Z. *et al.* Visual *β*-sheet-to-*β*-turn transition in luminescent polymeric vesicles for color-reporting drug delivery. *Angew. Chem. Int. Ed.* **64**, e202503875 (2025).

30. Wu, Z. *et al.* Dynamic cross-linked topological network reconciles the longstanding contradictory properties of polymers. *Sci. Adv.* **11**, e0825 (2025).

31. Webber, M. J. & Tibbitt, M. W. Dynamic and reconfigurable materials from reversible network interactions. *Nat. Rev. Mater.* **7**, 541-556 (2022).

32. Fang, Z. *et al.* 3D printing of dynamic covalent polymer network with on-demand geometric and mechanical reprogrammability. *Nat. Commun.* **14**, 1313 (2023).

33. Reith, M. A. *et al.* Sequence-dezined mikto-arm star-shaped macromolecules. *J. Am. Chem. Soc.* **144**, 7236-7244 (2022).

34. Reilly, L. T., Kottage, D., Cavallo, L., Falivene, L. & Chen, E. Y. Entropy-Regulated Selective Synthesis of Cyclic Polymers and Polycatenanes by Lewis Pair Polymerization. *J. Am. Chem. Soc.* **147**, 31689-31703 (2025).

35. Weil, T. & Chen, C. Cyclic polymers: synthesis, characteristics, and emerging applications. *Nanoscale Horiz.* **7**, 1121-1135 (2022).

36. Xu, C. *et al.* Regio- and sequence-controlled conjugated topological oligomers and polymers via boronate-tag assisted solution-phase strategy. *Nat. Commun.* **12**, 5853 (2021).

37. Yin, J., Choi, S., Pyle, D., Guest, J. R. & Dong, G. Backbone engineering of monodisperse conjugated polymers via integrated iterative

binomial synthesis. *J. Am. Chem. Soc.* **145**, 19120-19128 (2023).

38. Mills, H. A. *et al.* Sequence-defined conjugated oligomers in donor-acceptor dyads. *J. Am. Chem. Soc.* **145**, 23519-23526 (2023).
39. Li, Z. & Tang, Y. Article stair-like narrow N-doped nanographene with unusual diradical character at the topological interface. *Chem* **9**, 1-14 (2023).
40. Kim, M. P. *et al.* Iterative SuFEx approach for sequence-regulated oligosulfates and its extension to periodic copolymers. *Nat. Commun.* **15**, 3381 (2024).
41. Lai, Y. *et al.* Modulating ligand-exchange dynamics on metal-organic polyhedra for reversible sorting and hybridization of miktoarm star polymers. *Angew. Chem. Int. Ed.* **62**, e202311954 (2023).
42. Gkolfi, E. & Harmandaris, V. Soft character of star-like polymer melts: from linear-like chains to impenetrable nanoparticles. *Nano Lett.* **23**, 1608-1614 (2023).
43. Hu, R., Leung, N. L. C. & Tang, B. Z. AIE macromolecules: syntheses, structures and functionalities. *Chem. Soc. Rev.* **43**, 4494-4562 (2014).
44. Aida, T., Meijer, E. W. & Stupp, S. I. Functional supramolecular polymers. *Science* **335**, 813-817 (2012).
45. Zhang, G., Cheng, X., Wang, Y. & Zhang, W. Supramolecular chiral polymeric aggregates: construction and applications. *Aggregate* **4**, e262 (2023).
46. Wang, W. *et al.* Rapid automated iterative small-molecule synthesis. *Nat. Synth.* **3**, 1031-1038 (2024).
47. Xu, C., Dong, J., He, C., Yun, J. & Pan, X. Precise control of conjugated polymer synthesis from step-growth polymerization to iterative synthesis. *Giant* **14**, 100154 (2023).
48. Blair, D. J. *et al.* Automated iterative Csp^3-C bond formation. *Nature* **604**, 92-97. (2022).
49. Lehmann, J. W., Blair, D. J. & Burke, M. D. Towards the generalized iterative. *Nat. Rev. Chem.* **2**, 0115 (2018).

Acknowledgments

This work was supported by the National Natural Science Foundation of China (52525306 and 22375059), Shenzhen Science and Technology Innovation Program (JCYJ20220530160403008), and Natural Science Foundation of Hunan Province (2023JJ50002 and 2024RC1027). Thanks to the Analytical Instrumentation Center of Hunan University, and the AIE institute (www.aietech.org.cn) for providing technical assistance.

Author Contributions Statement

S.X., Z.Z., and B.Z.T. designed the research. Q.B., Ying Zhao, C.Z., Y.Z. 'affiliation 1', and Y.Z. 'affiliation 3' performed the research. Q.B., and S.X. conducted the analyses. S.X., Z.Z., and B.Z.T. supervised the research. Q.B., and S.X. wrote the paper. All authors substantially revised and edited the manuscript.

Competing Interests Statement

The authors declare no competing interests.

Tables

Table 1. Photophysical properties of **Pn** oligomers at different states.

	λ_{abs}, λ_{ex}/λ_{em} [nm] (Φ_F %)[a]			τ [ns] (k_r [10^8 s^{-1}], k_{nr} [10^8 s^{-1}]) [b]		α(AIE)[c]
	THF solution	Aggregate[d]	Powder	Aggregate[d]	Powder	
PL9	358, 391/530 (3)	393, 365/513 (66)	370, 403/543 (63)	3.1 (2.1, 1.1)	3.3 (1.9, 1.1)	18
PY12	363, 402/530 (2)	393, 365/513 (93)	370, 403/531 (96)	2.9 (3.2, 0.2)	3.4 (2.8, 0.1)	11
PX16	354, 391/530 (2)	387, 365/513 (83)	370, 403/525 (80)	3.3 (2.5, 0.5)	3.3 (2.4, 0.6)	13

[a]Absolute quantum yields measured by an integrating sphere. [b]k_r: radiative decay rate, k_{nr}: nonradiative decay rate. [c]Estimated by I/I_0, corresponding to Figure 6G/H/I. [d]Reprecipitation in 10 vol% THF/H_2O, corresponding to Figure 6C/D.

Figure Legends/Captions (for main text figures)

Figure 1. Schematic illustration of dynamic conjugated oligomer system with different topologies. (A) Dynamic chemistries of TAA building blocks. (B) Modular TPE-TPE interactions in supramolecular assembly. (C) 1D linear oligomer **PL9** showing dynamic conformations due to E-Z isomerization of TAA building blocks. (D) planar Y-type **PY12** and (E) stereo X-type **PX16** obtained using different core scaffold.

Figure 2. Iterative synthesis of precision conjugated Pn oligomers. Reaction condition for deprotection (D): [boronate] = 0.03~0.08 mM, NaOH (aq.) in THF/H_2O, 30ºC, 30 min. (A) Coupling (C) reaction condition for **3**, **4** and **5**: [boronate]:[**2**] = 3:1, $Pd(OAc)_2$, Sphos, K_3PO_4 in THF, 55ºC, 12 h. (B) Coupling (C) reaction condition for **PL9**: i) [**5**]:[**6**] = 2.2:1, $Pd(OAc)_2$, Sphos, NaOH in THF, 30ºC for 10 min; ii) H_2O (dropwise addition), 55ºC for 12 h. Coupling (C) reaction condition for **PY12**: [**5**]:[**7**] = 3.3:1, $Pd(OAc)_2$, Sphos, K_3PO_4 in 1.4-Dioxane, H_2O (dropwise addition), 90ºC for 12 h. Coupling (C) reaction condition for **PX16**: [**5**]:[**8**] = 4.4:1, $Pd(OAc)_2$, Sphos, K_3PO_4 in 1.4-Dioxane, H_2O (dropwise addition), 90ºC for 12 h. Purification (P) condition: flash silica gel chromatography with petroleum ether and dichloromethane as eluents.

Figure 3. Molecular characterization of Pn oligomers. (A/D/G) Chiral HPLC characterization of the constitutional isomer distribution for the pristine **PL9**(A), **PY12**(D), and **PX16**(G) solution. Inset: experimentally measured (left) and computationally simulated (right) MALDI-TOF HRMS characterization for **Pn**. (Column: CHIRALPAK IF Particle size 5 μm, Dimensions 4.6 mm × 250 mm, T = 30ºC, UV = 360 nm, concentration: 1×10^{-6} M, V = 20 μL, 50% isopropyl alcohol/*n*-hexane, flow rate: 0.1 mL/min). (B/E/H) 2D excitation-emission fluorescence spectroscopy of the pristine **PL9**(B), **PY12**(E), and **PX16**(H) in solution state (1×10^{-5} M). Inset: images under natural light (right) and 365 nm irradiation (left) in THF. (C/F/I) 2D excitation-emission fluorescence spectroscopy of the pristine **PL9**(C), **PY12**(F), and **PX16**(I) in powder state. Inset: fluorescence images of the powder under 365nm irradiation.

Figure 4. Dynamic interconversion of bifunctional TAA 2. (A) Reversible alkene isomerization of **2**-*Cis* ⇌ **2**-*Trans*. (B) Chiral HPLC characterization of TAA **2**, Column: CHIRALPAK IF particle size 5 μm, dimensions 4.6 mm × 250 mm, T = 30ºC, UV = 360 nm, concentration: 1×10^{-6} M, V = 20 μL, 20% *n*-hexane/isopropyl alcohol, flow rate: 0.1 mL/min. (C) Computational analysis of the **2**-*Cis* ⇌ **2**-*Trans* reaction.

Figure 5. Dominant molecular conformations and electrostatic surface potential (ESP) images of Pn oligomers by theoretical calculations. a) Conformation (left), front view (middle), and back view (left) of corresponding ESP images of the dominant **PL9** oligomer. b) Conformation (left), front view (middle), and side view (left) of corresponding ESP images of the dominant **PY12** oligomer. c) Conformation (left), front view (middle), and side view (left) of corresponding ESP images of the dominant **PX16** oligomer. Calculations were carried out at the CAM-B3LYP-D3/6-31G(d,p) level. Aliphatic chains and hydrogen atoms are omitted for clarity.

Figure 6. **Photophysical properties of Pn oligomers at different materials states.** (A/C/E) UV-vis absorption of **Pn** as (A) molecularly dissolved in THF solutions (1×10^{-5} M), as (C) disperse nanoaggregates in mixed 90 vol% water/THF solutions, and as (E) solid powder/films. (B/D/F) Corresponding steady fluorescence excitation (dot dash) and (solid line) emission spectra of **Pn** as (B) molecularly dissolved in THF solutions (1×10^{-5} M), as (D) disperse nanoaggregates in mixed solutions, and as (F) solid powder. Inset: fluorescence image in powder under 365 nm light irradiation. (G/H/I) Fluorescence spectra of (G) **PL9**, (H) **PY12**, and (I) **PX16** in series THF/water mixtures with different water fractions (f_w) and corresponding plots of relative emission peak intensity (I/I_0) versus f_w. I_0 was the peak intensity when $f_w = 0$. Inset: fluorescence image in solvents of $f_w = 0$ and 90 under 365 nm irradiation. Concentration: 1×10^{-5} M. Excitation wavelength: 370 nm.

Figure 7. Self-assembly of Pn oligomers. (A-C) AFM Characterization of assembled structures by evaporation of 1 μM toluene solution on silicon wafer for **PL9** (A), **PY12** (B), and **PX16** (C). (D-F) Corresponding SEM characterization of assembled structures by evaporation 1 μM toluene solution on silicon wafer for **PL9** (D), **PY12** (E), and **PX16** (F). Inset: TEM characterization of nanorods. (G-I) Positive fluorescence microscope characterization of assembled structures by evaporation of 10 μM toluene solution on clean quarz glass substrates for **PL9** (G), **PY12** (H), and **PX16** (I). Excitation wavelength: 330-380 nm. H: height, W: width, Tp: thread pitch. SEM samples were sprayed with platinum for 15 seconds to increase their electrical conductivity.

Figure 8. Molecular interactions in the supramolecular Pn assembly via MD simulation. (A) Molecular packing modelling of cell growth along the *b* axis of **PL9**-1 oligomer in the *P-1* space group, showing two molecules in a unit cell. (B) Molecular packing modelling of cell growth along the *c* axis of **PY12**-1 oligomer in the $P2_1$ space group, showing two molecules in a unit cell. (C) Molecular packing modelling of cell growth along the *a* axis of **PX16**-1 oligomer in the $P2_1$ space group, showing three molecules in a unit cell.

Editorial Summary

Topology is important for the properties of polymer materials, but can be difficult to control. Here, the authors report the development of conjugated oligomers with diverse topologies, each with distinct photoluminescence and photochemical properties.

Peer review information: *Nature Communications* thanks Anna Mielańczyk and the other, anonymous, reviewers for their contribution to the peer review of this work. A peer review file is available.